Highlights

Multichannel Electrochemical Impedance Spectroscopy and equivalent circuit synthesis of a large-scale vanadium redox flow battery

Journal of Power Sources xxx (xxxx) xxx

Andrea Trovò, Walter Zamboni, Massimo Guarnieri*

- A novel multichannel EIS measurements system for kW-scale RFBs is presented.
- Stray parameters of power connections affecting measurements were tackled.
- A stack equivalent lumped circuit was identified by means of EIS measurements.
- The dependence of the circuit parameters on the operating conditions was analyzed.
- This analyzer can be adopted in procedure for SOH evaluation of industrial RFBs.

Multichannel Electrochemical Impedance Spectroscopy and equivalent circuit synthesis of a large-scale vanadium redox flow battery

Andrea Trovò [a,b], Walter Zamboni [c], Massimo Guarnieri [a,b,*]

[a] *Department of Industrial Engineering, University of Padua, Padova, Italy*
[b] *Interdepartmental Centre Giorgio Levi Cases for Energy Economics and Technology, University of Padua, Padova, Italy*
[c] *Dipartimento di ingegneria dell'Informazione ed Elettrica e Matematica applicata (DIEM), Università degli studi di Salerno, Fisciano, Italy*

ARTICLE INFO

ABSTRACT

An original multichannel Electrochemical Impedance Spectroscopy (EIS) system operating at high bias current and suitable for kW-class Vanadium Redox Flow Batteries (VRFBs) is presented. Power and signal connections, whose stray parameters affected measurements, required a careful optimization and calibration in the implementation of the measurement chain. In any cases, electromagnetic interferences set an upper limit to the applied stimulus frequency that limited the set of measurement data at each bias point. The paper provides early results obtained with this EIS system, which were used to identify an equivalent circuit of the whole stack in which each cell is represented with a dynamic Thévenin equivalent, i.e. the series of a voltage source, a variable resistor and a variable RC loop. The dependence of the equivalent parameters on the operating conditions has been experimentally analyzed, confirming that only the RC-loop resistance is strongly affected by mass transport. To our knowledge, this is the first dynamic equivalent circuit of a whole stack that has been validated against EIS measurements taken on a real industrial-scale VRFB. Building on the measurement methodology here presented, advanced online state of health of industrial flow batteries can be developed and implemented.

1. Introduction

Renewable energy sources, particularly wind and solar radiation, are widely regarded as the most promising solutions to address fossil fuels depletion and global heating [1] and extensive research programs aim at matching the increasing power demand with such intermittent sources [2]. In grid applications, energy storage allows one to cope with the daily fluctuations of power demand with the intermittent nature of renewable sources [3]. Several technologies can be used to address these problems in addition to pumping hydro, e.g. compressed air, flywheels, supercapacitors, electrochemical devices [4] and hydrogen [5]. Redox Flow Batteries (RFBs) are a promising option, thanks to their intrinsic advantages, such as independent power and energy sizing, good energy efficiency and long-life cycle [6]. Among various types of RFBs, the most researched and successful technology at present is the all-Vanadium Redox Flow Batteries (VRFBs) [7], but other RFB systems such as hydrogen-bromine [8], zinc-bromine [9], and organic electrolyte chemistry [10] are also actively researched. Twenty-six companies manufacture VRFBs [11], and several plants with rating exceeding some MW and MWh have been commissioned [12]. The principle of this technology is well known, but more development is needed to build high performance industrial-scale plants. Currently, progress in this field is limited by the scarcity of engineering studies on cell and stack design, reaction environment, control strategy, and their relationship to performance and efficiency [13–15]. As a matter of fact, most studies are carried out on small single cells with the aim of characterizing and optimizing the materials used in the battery, i.e. electrodes [16,17], membranes [18,19], bipolar plates [20,21] and electrolytes [22,23].

Electrochemical Impedance Spectroscopy (EIS) is widely used to investigate various kind of properties and degradation phenomena occurring in electrochemical systems [24]. With regards to the use of EIS in RFBs, the majority of published works are restricted to short term studies of small cells in the laboratory and, to the best of authors' knowledge, the direct use of this technique on pilot-scale plants has not yet been documented. This paper aims to fill this gap by describing the implementation of a multichannel EIS measurement system on an Industrial-Scale VRFB (IS-VRFB), with a rated power/energy of 9 kW/27 kWh and by reporting early results. This multichannel analysis can be important in multi-cell stacks, because it is able to reveal unbalances and the incorrect simultaneous feeding of all cells. Indeed, last

cells might have insufficient flow at high power and their performance could be compromised. In addition, the continuous monitoring of EIS parameters and their evolution allows one to detect a premature aging and constitute a valuable advantage of the method. In these measurements, stray parameters, like wiring inductances and resistances, affected measurements and made the diagnostic procedure quite challenging to implement. On the one hand, the stack size imposed longer electrical connections which needed a much trickier optimization than small single cells, being affected by larger electromagnetic interferences (EMIs) from external devices. On the other hand, the stack had to be operated at high bias currents, which generated non-negligible conducted disturbances. Such challenging measurements aimed at identifying potential critical operating conditions and at driving clues for optimizing cell design. The paper is structured as follows. Section 2 presents the main features of EIS and the published state of the art of its applications to VRFBs. Section 3 describes the IS-VRFB test facility on which measurements were conducted, with a focus on its multichannel EIS analyzer, calibration procedure and the wiring optimization. In Section 4 an equivalent lumped circuit and its validation are reported. Numerical and experimental results are also discussed. The effect of the battery State Of Charge *SOC*, electrolyte flow rate *Q* and current *I* on the lumped circuit parameters are also highlighted. Finally, conclusions are given in Section 5.

2. EIS: background and VRFB applications

2.1. Background

The EIS has been taken to maturity since about six decades [25] and is now widely used in testing electrochemical devices such as batteries, supercapacitors and fuel cells [26–28]. The success of EIS in many kind of analyses mainly depends on two reasons. First, with sinusoidal or narrow-band stimuli, it allows one to precisely activate processes with a given characteristic time, detecting individual process contributors, that is, ohmic resistance, interfacial charge-transfer resistance, mass transport resistances in the catalyst layer and back-diffusion layer, in a relatively short measurement time. The second important aspect is that it can help identifying potential problems or failures within the system under test [29].

In fact, it is used to characterize electrodes, interfaces and materials properties, to assess the *SOC* and State Of Health (*SOH*) of rechargeable batteries, modules or packs and the *SOH* and degradation in supercapacitors and fuel cells. In addition, EIS is used at system level for monitoring, diagnostic and fault detection purposes in several applications [30–32].

The strategy of EIS characterization of electrochemical devices, electrodes or materials, consists in applying a small electrical stimulus superimposed to a dc bias operating condition, measuring the device response using a four-wire measurement method, and, finally, computing a suitable voltage-to-current ratio in the frequency domain. The typical stimulus is purely sinusoidal, repeated sequentially at different frequencies in a range that varies with the scope of the analysis and type of device and may extend up to a range from 1 mHz to 1 MHz. An appropriate signal processing, often based on the Fourier transform, helps extract the fundamental harmonics at the test frequency *f* from both input and output signals, to get rid of possible noise.

The EIS experiment is often performed on half-cells, electrodes, and single cells with small active areas. However, in industrial-scale applications, cells with large cross sectional area are used in stacks and battery packs are highpowered, so that taking EIS measurements is a much more challenging issue than usually reported in the literature. In these cases, a variable electrical load bank can be used profitably to apply a bias condition to the device under test. The ac stimulus is added and together with the corresponding response are sent to the EIS analyzer to compute the impedance $Z(\omega)$ with $\omega = 2\pi f$.

This approach suffers from a signal degradation at high currents due to the stray parameters of the power wires, which limits the maximum frequency to a few kilohertz. In some works on heavy-duty applications for fuel cells, the upper frequency limit is extended to 20 kHz, but in the presence of a loss of accuracy in the response of the load bank that impacted on the results [29].

2.2. EIS-derived models

In many researches, the EIS spectrum is used to fit a specific model, identifying a few parameters characterizing the dynamics of the electrochemical system [33]. A wide variety of models have been proposed in the literature to describe processes with long characteristic times, such as thermal transport, as well as those with short characteristic times, such as gas diffusion. Various reviews have been published, e.g. [30,34,35], the latter treating aspects of EIS applied to VRFBs.

In order to face system-level problems, very often circuit model of the measured impedance $Z(\omega)$ are used, which are characterized by various degrees of complexity. This models must present easy parametrization, span over wide frequency ranges, and allow a sufficient physical insight. These models include linear resistors, capacitors, inductors and special elements, such as the Warburg element and the Constant Phase Elements (CPE). Despite the linear condition of the frequency-domain investigation, the resulting complex impedance is far from being synthesized with lumped parameters that results in linear circuits in time domain. Therefore, simplifications are advisable, especially for system-level applications, unless a high order linear circuit must be specifically implemented to represent the device. As far as system level targets are aimed, simple few-states linear resistive–capacitive circuits (RC models) may satisfactorily be used [35,36]. Usual dynamic lumped equivalent of electrochemical cells consist of the series of a voltage source, a resistance and one or more RC loops, which are also used in various time-domain simulations [37]. As regards VRFBs, a single RC loop per cell was used by Zhang et al. [38], in studying a 1 kW/1 kWh VRFB developed by Kim et al. [39]. Wei et al. coupled such a model with an online identifier to predict the VRFB *SOC* [40], and used it also for real-time monitoring of the capacity loss [41].

In order to extract the parameters of the circuit model, both the shape of the impedance plot and the frequency of each measurement are fundamental. Various techniques can be implemented or used for the identification of the impedance parameters based on the EIS response. Deterministic approaches are available in commercial software suites for personal computers, like Matlab®, and are useful in offline analyses. For online or onboard identification, strict requirements in terms of computational burden or memory may make preferable alternative approaches, like those based on evolutionary programming [42].

2.3. EIS applications to VRFBs

In the case of VRFBs, the use of EIS has been mainly devoted to the analysis of single cells with small electrode surfaces, aimed at investigating cell or material properties, rather then to face system-level issues of large batteries. Therefore, most of the recent literature deals with low current tests [43–48]. Sun et al. conduced EIS studies on VRFB single-electrodes using a dynamic hydrogen reference electrode [43]. The same research group used EIS to measure and resolve the ohmic, charge transfer and diffusion overvoltages at the negative electrode of a VRFB as functions of the current density, identifying the parameters of the equivalent circuit [44]. Derr et al. used half-cell and full-cell EIS measurements to analyze the electrochemical degradation of carbon felt electrodes at different *SOC* [45]. In a successive work [46], the same authors analyzed the electroless chemical aging of the same electrode through the changes of the charge transfer resistance and of the double layer capacitance, determined with EIS. In this kind
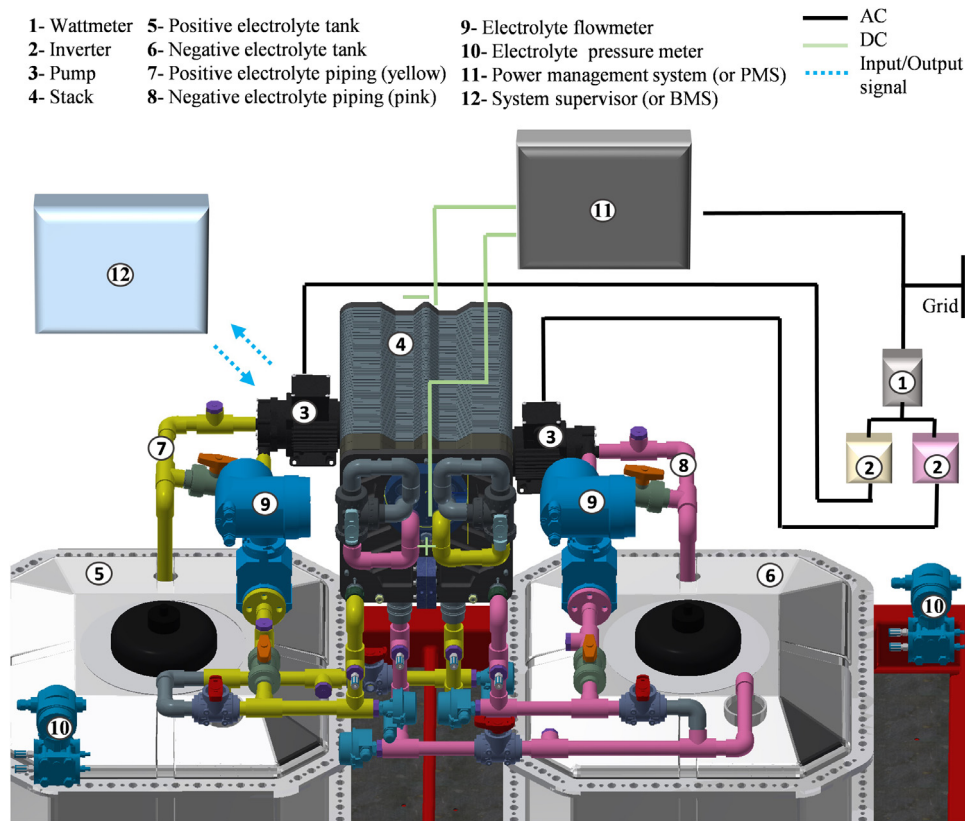
Fig. 1. The 9 kW/27 kWh IS-VRFB test facility with its main components, on which EIS measurements were performed.

of works, the EIS spectra are typically fitted with impedance models including CPE and Warburg elements. The current level is always low, helping to minimize to a negligible level parasitic phenomena which instead are significant in large batteries operating at high currents. In [47], Pezeshki et al. used EIS to quantify the charge transfer, mass diffusion, and ohmic overpotentials in a VRFB, using the model defined in [44]. Becker et al. combined EIS with polarization curves (*V* vs. *I*) for the characterization of a porous electrode in a VRFB under various operating conditions [48].

Messaggi et al. analyzed a 10-regions macro-segmented cell with a 25 cm^2 active area by means of EIS to obtain impedance spectra, as well as the polarization curve resolved at active area level [49]. Both positive and negative symmetric cells for all-vanadium configuration where studied. This investigation shed new light on the inhomogeneous distribution of electrolyte over the porous electrode. Despite the structure was more complex than in the previous papers, the latter approach is still far from being suitable for high-power applications.

A recent paper by Li et al. investigated the suitability of VRFBs for power quality control applications, even if the tests were made on a laboratory scale cell, [50]. Experiments were carried out under different operating conditions and time-domain transient measurements were fitted with complex-valued impedance models through a fractional order computational approach. EIS was used to validate the identification results, highlighting that CPE and Warburg elements, as well as two semi-cell loops, helped achieving accurate model fitting. Manschke et al. resorted to EIS to test the functionality of RFBs which used alternative and non-toxic chemistries [51]. The EIS measurements were performed on full-size batteries with large electrodes and multiple cells, thus proposing a qualification method for these batteries. The EIS measurements were able to detect deliberately manipulated cells.

Although the aforementioned single-cell low-current EIS investigations reported widely different measurements, these kind of analyses are still embryonic and far from being conclusive for applications of practical interest, with kW-class VRFBs.

3. The experimental plant

3.1. IS-VRFB test facility

The IS-VRFB test facility has been designed and built to study the engineering issues of large-scale VRFB systems and their interface with the grid [52]. Its stack consists of 40 cells with 600 cm^2 active area and with a conventional topology, i.e. with series electric and parallel hydraulic connections. The cells are made of a Nafion® 212 membrane and two 5.7-mm thick graphite felt electrodes. The 550-L-each electrolytes consist of 1.6M vanadium dissolved in 4.5M sulfate solutions. Two closed hydraulic circuits allow circulating the electrolytes between stack and tanks (Fig. 1).

The centrifugal pumps (PMD-641 by Sanso) are driven by two inverters (DC1 by Eaton) providing a flow rate modulation based on a feedback control managed by the Battery Management System (BMS) [53]. The electric power conditioning in charge and discharge relies on a Power Management System (PMS) made with an ac/dc bidirectional static converter (by Dana) rated ±75 A dc and 0–85 V dc on the battery side. It can be controlled either locally or remotely by the BMS. A variable passive load allows high current discharges up to 600 A.

The facility is instrumented with two flow meters, two differential pressure meters, two tank level meters and seven resistance temperature detectors (RTDs) (Fig. 1). Alloy C276 rheophores, placed in contact with the cell graphite bipolar plates, detect cell voltages which are sent to the BMS via galvanic isolators (Verivolt IsoBlock). Stack voltage s measured by a LEM CV 3-100/SP3, while a LEM HASS 50-S and a LEM HASS 200-S detect the stack current in two different ranges, covering 0–600 A. Noise suppression is ensured by a grounding system built around a large copper equipotential bar that provides a common reference. All signals are treated and normalized in a compact data acquisition device (Compact DAQ 9179 by Nationals Instruments). Acquisition and control functions are performed by an in-house software
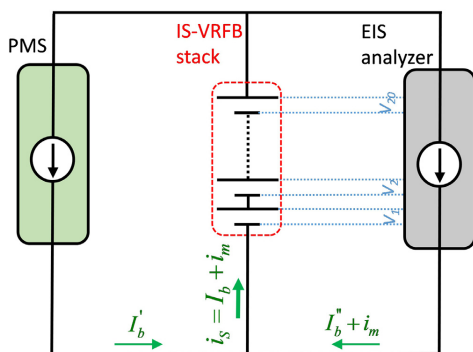
Fig. 2. Equivalent electric circuit of the multichannel EIS measurements test on IS-VRFB stack.

Table 1
Technical datasheet of MMulty SP EIS analyzer.

Description	Value
Number of channels	20
Limiting voltage	100 V
Limiting bias current I_b	100 A
Limiting power losses	1500 W (with water cooling) 800 W (with air cooling)
Limiting current signal I_m	$\leq 10\% \ I_b$
Nominal frequency range	$0 - 100$ kHz
Impedance measurement accuracy	$\pm 0.2\%$ at full scale

1 package implemented in LabVIEW 2016 (Nationals Instruments). This
2 environment is based on a state-machine architecture that allowed
3 flexible implementation of routines for the automatic control of the
4 experiment [54]. In particular, a PID controller was developed to
5 achieve a precise feedback flow-rate control in each pump fed by
6 the comparison of dynamically BMS-generated settings with the flow-
7 meter signals. The hardware and software implementing the signal
8 conditioning, processing and the experiment control constitutes the
9 BMS [55]. The IS-VRFB has already achieved current densities as high
10 as 665 mA cm^{-2} and 583 mA cm^{-2} in fast response and steady-state
11 conditions, respectively [56].

12 *3.2. EIS equipment*

13 A multichannel EIS was carried out with an ad hoc designed EIS
14 analyzer (MMulty SP by Materials Mates Instruments) that is capable
15 of a theoretical frequency range $f = 0-100$ kHz. Twenty cells could be
16 tested simultaneously by using this analyzer. The electric scheme of the
17 stack and the EIS analyzer used in these tests is shown in Fig. 2. A real-
18 time control system monitors and controls the EIS measurements. The
19 core of EIS analyzer consists of a waveform generator and a frequency
20 response analyzer. It can operate either in galvanostatic mode (that is,
21 as harmonic current source) or in potentiostatic mode (as harmonic
22 voltage source). The galvanostatic mode was used and the $i_m(\omega)$ stimuli
23 at angular frequency $\omega = 2\pi f$ were added to a common bias dc load
24 current I_b. In every measurement sequence I_b was kept constant to set
25 the cell operating point at which the EIS analysis was done, while the
26 frequency was varied in a sequence of values in a selected range.
27 Measurement sequences were repeated at different bias I_b and
28 different amplitudes I_m of the stimuli harmonic current, and were
29 processed to select the best measurement condition at which the
30 impedance $Z(\omega)$ was extracted. At the same time the Fourier analysis
31 of the stimulus and output signal was performed to verify the absence
32 of excessive distortion.
33 Measurements over specified frequency ranges at every I_b were
34 automatized by a customized procedure that allows the user to select
35 the best gain to bandwidth ratio.
36 The EIS waveform generator is capable of producing different stim-
37 ulus waveforms, and, in particular, sinusoidal waveforms, in a selected
38 sequence of frequencies. The stimulus can be added to an external I_b'
39 and/or internal I_b'' to form the dc bias current I_b. These features allow
40 one to operate the EIS at load currents between 15 A and 90 A. The
41 main features of the MMulty SP EIS analyzer are listed in Table 1.

42 *3.2.1. Preliminary calibration*
43 A major issue in performing accurate EIS test is the minimization
44 of stray parameters, like wiring inductances and resistances, which
45 may jeopardize the cell impedance, particularly at high frequencies.

46 In the case of small single cells, such minimization can be achieved
47 by properly choosing the cables, reducing their lengths and reciprocal
48 distance and optimizing the design of their connection to the cell and
49 EIS device. Conversely, wiring optimization is a much more elusive
50 target in the case of a large stack, made with many cells and carrying
51 much higher currents, as is the case of IS-VRFB, which required long
52 cables with a large cross section. Wiring of this size may pick up EMIs,
53 particularly at high frequencies. In order to assess their effect, some
54 preliminary tests were performed, in which the known impedance of
55 given test circuits, made with calibrated resistances and capacitors,
56 were measured with the EIS analyzer. The key points of such calibration
57 tests are reported hereafter.

58 • A poor accuracy of the EIS analyzer was observed in the case of
59   a test circuit with a small resistance (0.01–0.1 Ω) and a relatively
60   large capacitance (1–20 mF). This effect was attributed to the
61   wiring inductance that is not negligible with respect to the whole
62   measurement chain in the frequency range of interest.
63 • It was found that the solid-state PMS and the pump inverters were
64   a major cause of the external noise over a frequency range of
65   0–60 kHz. A compromise between gain and bandwidth in the
66   analyzer settings provided the best results, with minimized EMIs.
67 • In addition, the circuits were tested to detect possible differ-
68   ences among the 20 measurement channels, finding negligible
69   deviations.

70 *3.3. VRFB stack wiring optimization*

71 A stripboard allowing minimized wiring length was installed atop
72 the stack as close as possible to the cell voltage pickups (Fig. 3). It
73 dispatches the cell voltages to the EIS analyzer, to the BMS, and to a
74 local LED voltage display. The current signal wiring was made with a
75 twisted pair together in order to reduce the stray inductance as much as
76 possible (Fig. 3). A litz-like multistrand wire for the power connections
77 demonstrated to produce the best results as regards minimization of
78 stray inductances and related EMIs, [57]. In conclusion, the major
79 issues in performing EIS on the IS-VRFB stack were found in the electri-
80 cal connections and their inductive nature, which produced increasing
81 interference with increasing frequency.

82 **4. Results and discussion**

83 *4.1. Equivalent circuit*

84 The lumped model representing the 40 cells was a trade-off between
85 model complexity and accuracy. Each cell was represented as a voltage
86 source, a linear resistor and a single RC loop [37], (Fig. 4).
87 This equivalent circuit was used to study the steady-state operation
88 of an industrial RFB stack under different operating conditions, nev-
89 ertheless, it can investigate also the transient behavior. The voltage
90 source E_0 is the open circuit voltage given by the Nernst equation [58].
91 The resistance R_o accounts for the cell ohmic losses due to mem-
92 brane, electrodes, electrolytes and bipolar plates. Experimental and
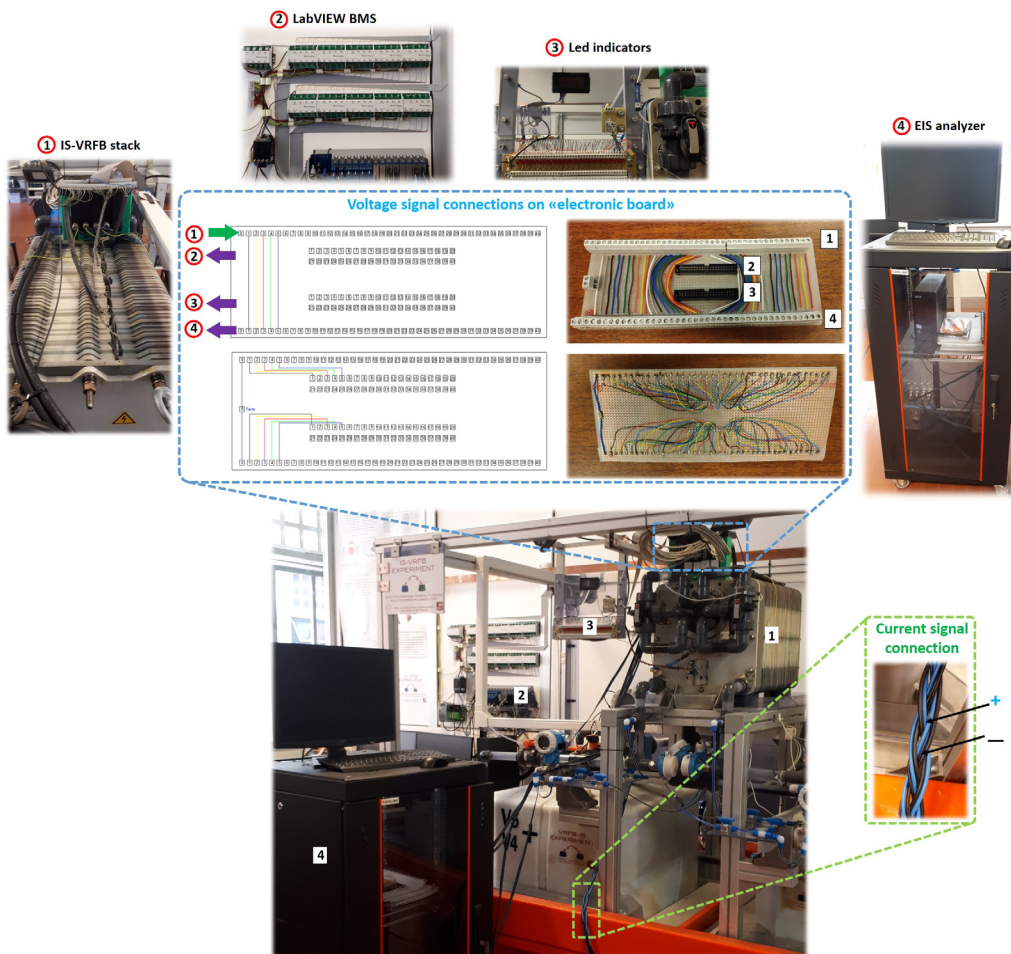
Fig. 3. Components of the voltage and current circuits used for EIS measurements. The voltage signals are led to a stripboard atop the stack consisting of four terminal strips: (1) connections to the 40-cell pickups, (2) connections to the LabVIEW BMS, (3) connections to the local LED display, (4) connections to the EIS analyzer. The current wiring was made with a litz-like cable, in order to reduce the stray inductance.

numerical investigations in steady-state conditions, previously developed by Guarnieri et al. in [59], revealed that the electrodes soaked with electrolytes provide the major contribution to R_o, i.e. at least 70%, while the membrane contributes for about 20%, and, finally, the graphite bipolar plates for about 10%. The resistance R_{at} is a non-linear resistance which takes into account the activation and concentration overpotentials. It depends on the cell current, SOC and electrolyte rate Q, as shown in [59]. The cell capacitance C_{dl} represents mainly the electrical double layers that appears at the interfaces between porous electrodes and liquid electrolytes [60]. Shunt currents were not taken into account because they did not affect the accuracy of the fast response analysis, being one order of magnitude lower than the stack current I_s [61].

The model depicted in Fig. 4 is the simplest one to study the main dynamics of the system in a frequency mid range, in which only one arc appears in the Nyquist plot [62]. Consequently, the model synthesizes the cell impedance with only three elements. It is well-known that a so-called Zarc element, that is a parallel loop of a resistor and a CPE, could replace the RC loop to better describe the typical arc depression by using one more parameter [33]. This approach has three main drawbacks for the application discussed in this paper. First, one more degree of freedom in the identification may not be convenient in the presence of spectra characterized by few experimental points, like some of those considered hereinafter. Moreover, the choice of a more complicated model is not recommended in literature if the spectra are already well fitted by a simpler approach, as clearly claimed, for instance, in [26]. Finally, the RC model can also be used as it is in the

time domain, while the Zarc element would require a more complicated mathematics, such as the fractional order calculus, to extract its time domain response. For all these reasons, the authors preferred to use the linear RC model of the cell impedance, avoiding CPE and Warburg elements. In is worth to consider that the RC model allows one to easily compute both the high-frequency resistance, that is R_o, and the equivalent series resistance of the VRFB, that is shown to be related to the battery cyclic aging, as it is for other electrochemical devices. For instance, Daugherty et al. have shown this for VRFB in the presence of various kind of high-performance electrodes in [17].

4.2. Model parameter identification

The cell passive elements of Fig. 4 which form the cell impedance $Z_{\text{mod}}(\omega)$:

$$Z_{\text{mod}}(\omega) = R_o + R_{at} \frac{1 - j\omega R_{at} C_{dl}}{1 + (\omega R_{at} C_{dl})^2}, \tag{1}$$

and are contained in the vector $U = [R_o, R_{at}, C_{dl}]$ were identified by means of the optimization algorithm [63]:

$$U = min \sum_{i=1}^{N_f} |Z_{\text{exp}}(\omega) - Z_{\text{mod}}(\omega)|, \tag{2}$$

where $Z_{\text{exp}}(\omega)$ is the experimental impedance provided by EIS analyses and N_f is the number of sampled frequencies. This optimization problem was solved with a Matlab® nonlinear optimization algorithm.
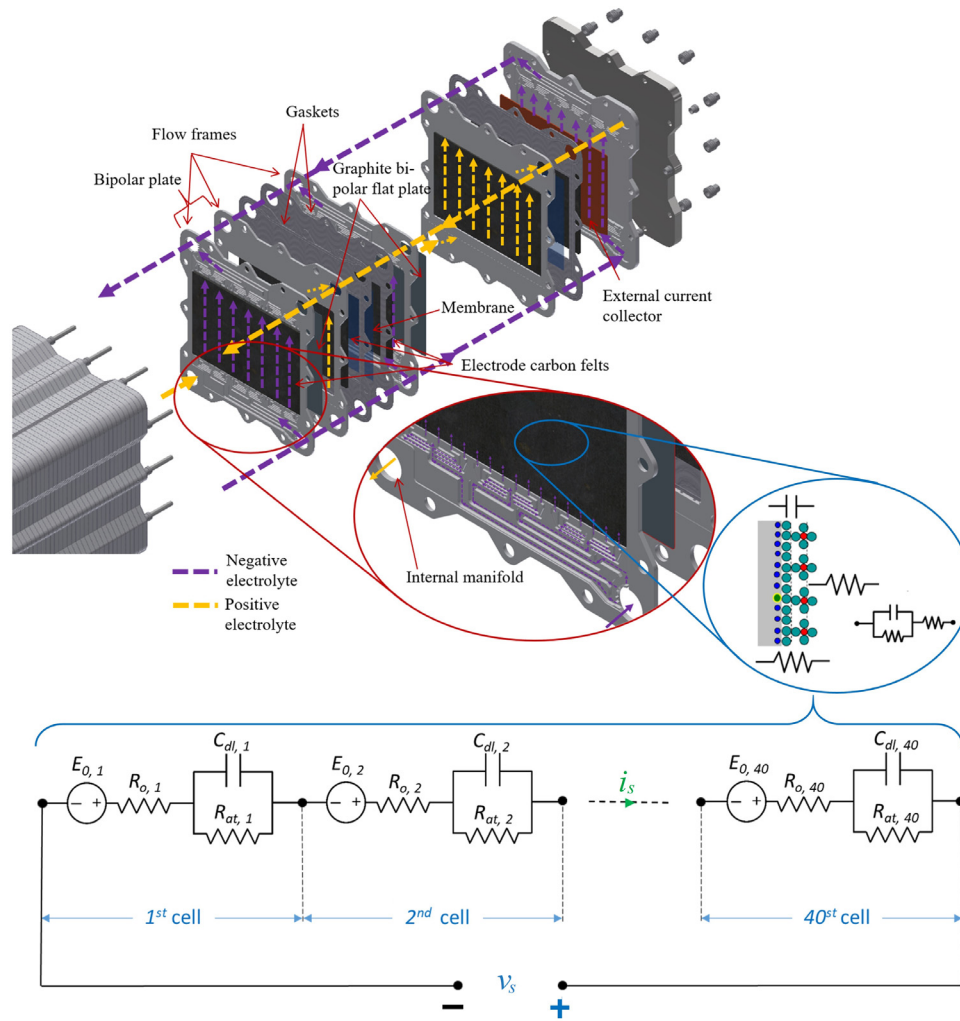
Fig. 4. Lumped circuit of IS-VRFB stack. Each cell is composed by a voltage source E_0, an internal resistance R_o in series with a first order RC pairs (R_{at} and C_{dl}).

The previous investigations was repeated at different values of SOC, Q and I_b with the same stimulus amplitude $I_m = 0.8$ A, in the frequency range between 0.5 Hz and 6 kHz. The upper frequency limit was chosen to ensure measurement accuracy against the EMI issues described above, in agreement with the EIS analyzer manufacturer recommendations.

In must be noted that the 6 kHz limit is usually sufficient to build full EIS plot in which the high frequency end matches the abscissa axis [50], nevertheless this may not be the case for large cells, due to the inherent values of the resistive and capacitive parameters representing mass transport and double layer events inside the cells, as we will comment further on.

4.3. Early results

Early experiments were devoted to validate the equivalent circuit of Fig. 4. With the aim of investigating how transport losses affect the circuit parameters, several tests were performed at different flow factor α which is given by the ratio between the flux of charges provided by the electrolyte flow to the electrochemical reactions and the charge rate effectively produced by the reactions:

$$\alpha = \frac{Q F c_V (1 - SOC)}{N I_b} \quad \text{(charge)} \quad (3)$$

$$\alpha = \frac{Q F c_V SOC}{N I_b} \quad \text{(discharge)} \quad (4)$$

with $F = 96\,485$ C mol^{-1} the Faraday constant, $N = 40$ is the number of cells in the stack, and $c_V = 1600$ mol m^{-3} is the vanadium total concentration. In addition, by varying the initial SOC and bias load current I_b, the influence of the ohmic and activation losses is respectively analyzed.

For the sake of simplicity, Fig. 5 shows the experimental and numerical Nyquist and Bode plots of cell no. 10 only, at different setting:

(a) $I_b = 35$ A, $SOC = 30\%$, $Q = 10$ L min^{-1} (i.e. specific flow rate $q = 6.9 \cdot 10^{-3}$ cm s^{-1});
(b) $I_b = 10$ A, $SOC = 30\%$, $Q = 20$ L min^{-1} ($q = 13.8 \cdot 10^{-3}$ cm s^{-1});
(c) $I_b = 35$ A, $SOC = 30\%$, $Q = 20$ L min^{-1};
(d) $I_b = 10$ A, $SOC = 60\%$, $Q = 20$ L min^{-1};
(e) $I_b = 80$ A, $SOC = 60\%$, $Q = 20$ L min^{-1}.

These operating conditions were chosen to produce flow factors in a wide range (between 5.5 and 77). For each setting, the EIS impedance was determined at several frequencies shown by blue circles in Fig. 5. The average duration of each frequency sequence is about 30 min, that is 2 min per frequency, allowing a SOC variation not exceeding 4%, due to electrolyte discharging [64].

The diagrams at $SOC = 30\%$ indicate values of R_o higher than those at $SOC = 60\%$. This behavior is due to electrolytes which fill the electrode pores and to the higher conductivities $\sigma_V = 41.3$ S m^{-1} and $\sigma_{II} = 27.5$ S m^{-1} of the positive and negative charged electrolytes, with
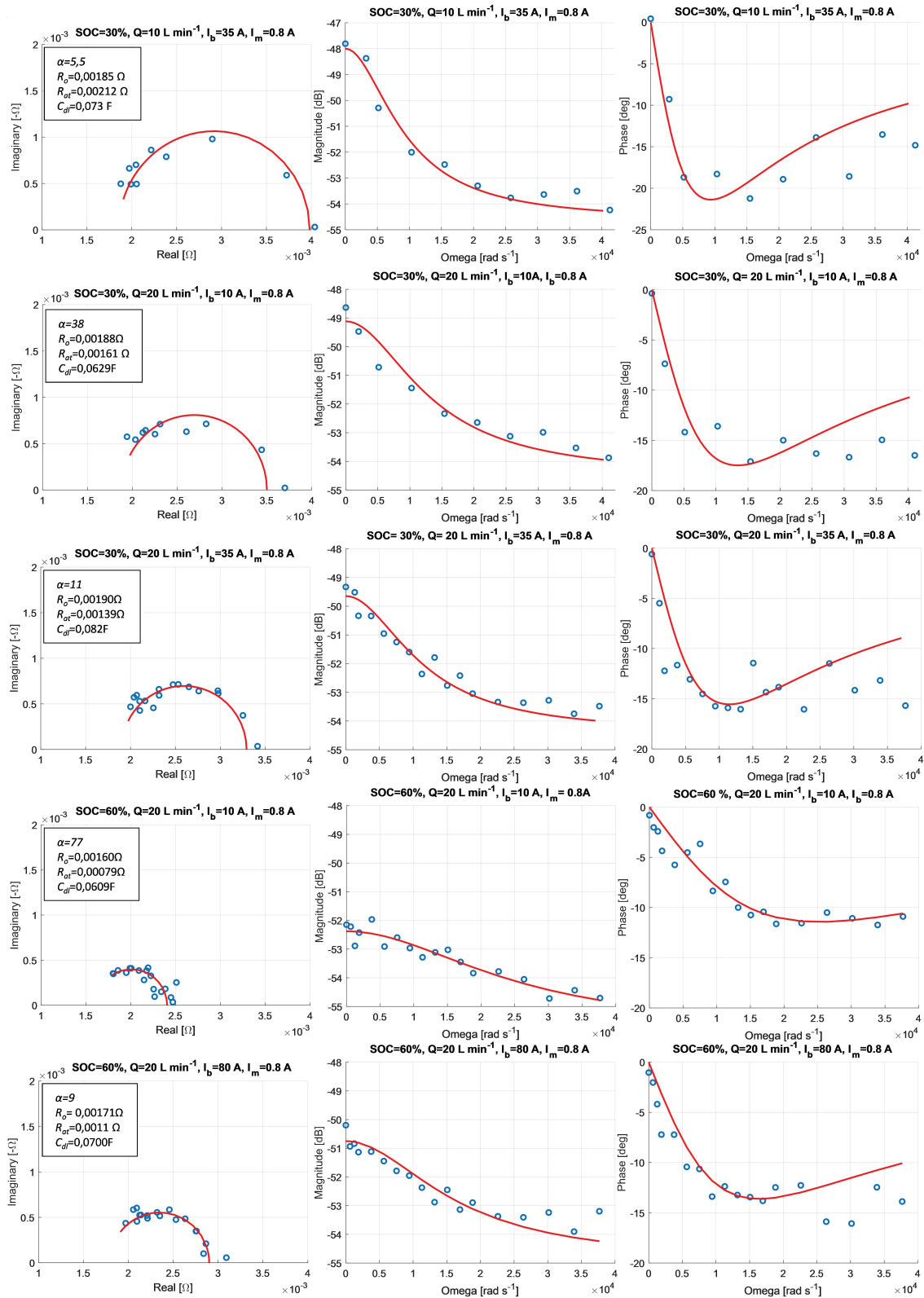
Fig. 5. IS-VRFB: impedance (Nyquist and Bode plots) of the 10th cell out of 40 in the frequency range 0.5 Hz–6 kHz with a stimulus amplitude of I_m = 0.8 A, SOC = 30%, 60%, Q = 10 L min^{-1}, I_b = 10 A, 35 A, 80 A. The corresponding flow factor range was α = 5.5–77. Tests were performed at a constant room temperature T = 21 °C.

respect to σ_{IV} = 27.5 S m^{-1} and σ_{III} = 17.5 S m^{-1} of the corresponding discharged species.

The diagrams of Fig. 5 show also that R_{at} = 2.12 mΩ at SOC = 30%, Q = 10 L min^{-1} and I_b = 35 A, i.e. at α = 5.5, and R_{at} = 1.39 mΩ at the same testing conditions except double Q, i.e. α = 11). Since

I_b mainly affects activation losses, SOC mainly affects ohmic losses and SOC and I_b are the same in the two cases, such difference in R_{at} is due to transport losses. This evidence is consistent with the results reported in [59], which highlights that transport losses are important as long as α is lower than a value α_k at which polarization curves converge to

Table 2

Average values and standard deviations of the identified parameters of the IS-VRFB stack at frequency range from 0.5 Hz to 6 kHz, with variable flow factors α between 5.5 and 77, by varying the initial $SOCs$, bias load current I_b and electrolyte flow rates Q, at stimulus amplitude I_m =0.8 A. The tests were performed at a constant room temperature T =21 °C. In the last three rows, σ stands for standard deviation.

SOC [%]	30	30	30	30	30	60	60	60
Q [L min^{-1}]	10	10	20	20	20	20	20	20
I_b [A]	10	35	10	35	60	10	35	80
α [–]	19	5.5	38	11	6.5	77	22	9
R_o [mΩ]	1.85	1.88	1.79	1.80	1.90	1.61	1.63	1.675
R_{at} [mΩ]	1.45	1.94	1.48	1.53	1.71	0.82	0.9	1.13
C_{dl} [mF]	65.7	65.9	61.9	68.6	69.3	67.6	60.3	68.5
σ_{R_o} [mΩ]	0.159	0.106	0.122	0.190	0.230	0.120	0.157	0.185
$\sigma_{R_{at}}$ [mΩ]	0.176	0.198	0.150	0.194	0.197	0.094	0.089	0.142
$\sigma_{C_{dl}}$ [mF]	13.4	9.899	11.257	15.736	9.369	8.451	6.924	5.472

the same minimal-slope linear profile. This α_k is a weakly increasing function of SOC, being $\alpha_k = 12$ at $SOC = 30\%$ and $\alpha_k = 14$ at $SOC = 80\%$. Increasing α beyond α_k only results in a useless hydraulic losses. Conversely, transport losses increase as α becomes smaller and smaller than α_k. For the sake of example, at $\alpha = 5.5$ corresponding to $\alpha_k = 12$ and $R_{at} = 2.12$ mΩ exceeds $R_o = 1.85$ mΩ, while, at $\alpha = 11$, that is close to $\alpha_k = 12$, $R_{at} = 1.39$ mΩ is smaller than $R_o = 1.90$ mΩ. Finally, C_{dl} remains fairly constant in all tests. This capacitance arises from the double layer at the surface electrode interface (SEI), and there is a consensus in the literature that it depends on the electrolyte flow condition within the porous felts. Advanced simulations based on CT meso-scale medium reconstruction and lattice-Boltzmann and Lagrange particle tracking methods have shown that the flow remain laminar with minor changes within the pores [65], confirming the minor variability of C_{dl} observed in our tests.

Similar considerations can be drawn by analyzing the results of Table 2, which shows the average values of the identified parameters among the first 20 cells out of 40 at varying operating conditions.

Fig. 5 shows that at the upper frequency limit of $f_{\max} = 6$ kHz all plots are quite far from matching the abscissa axis. In fact, introducing $\tau = R_{at}C_{dl}$, and given the loop impedance:

$$Z_{RC} = R_{at}\,\frac{1 - j\omega\tau}{1 + (\omega\tau)^2},\tag{5}$$

such matching imposes $\omega\tau \gg 1$, whereas the parameters synthesized for IS-VRFB (Table 2) roughly approach this condition at the maximum frequency: $2\pi f_{\max}\tau \approx 2.2$, due to the size and physical–chemical properties of its electrodes.

R_{at} drastically decreased with SOC at fixed Q and I_b, e.g., it was found $R_{at} = 1.48$ mΩ at $SOC = 30\%$ and $R_{at} = 0.82$ mΩ at $SOC = 60\%$, both at $Q = 20$ L min^{-1} and $I_b = 10$ A. This strong dependence can be ascribed to the different viscosities of the vanadium species, and thus of the electrolytes at varying SOC, because viscosity affects the diffusion coefficient that govern electrolyte transport. To confirm this correlation, the kinematic viscosity of the electrolytes was measured by means of a U-tube reverse flow viscometer BS/IP/RF - size 2 (by PSL Rheotek). It was found that the viscosity of the positive electrolyte containing V(V) and V(IV) showed a small decrease at increasing SOC, being ca. 3.45 mm^2 s^{-1} at $SOC < 40\%$ and 3.06 mm^2 s^{-1} at $SOC \geq 60\%$. Instead, the viscosity of the negative electrolyte containing V(III) and V(II) presented a significant decrease at increasing SOC, being ca. 5.45 mm^2 s^{-1} at SOC < 30% and dropping at 3.71 mm^2 s^{-1} at $SOC = 90\%$. A similar strong decrease of the viscosity the negative electrolyte at increasing SOC was found by Li et al. [66].

Different groups of cells were then tested in the same conditions as those in Table 2 and no significant discrepancies were found. Since R_{at} depends on the electrolyte flow rate, these minimal discrepancies proved the homogeneity of the electrolyte flow rate among cells. Similar considerations can be drawn for R_o that, being dependent on the
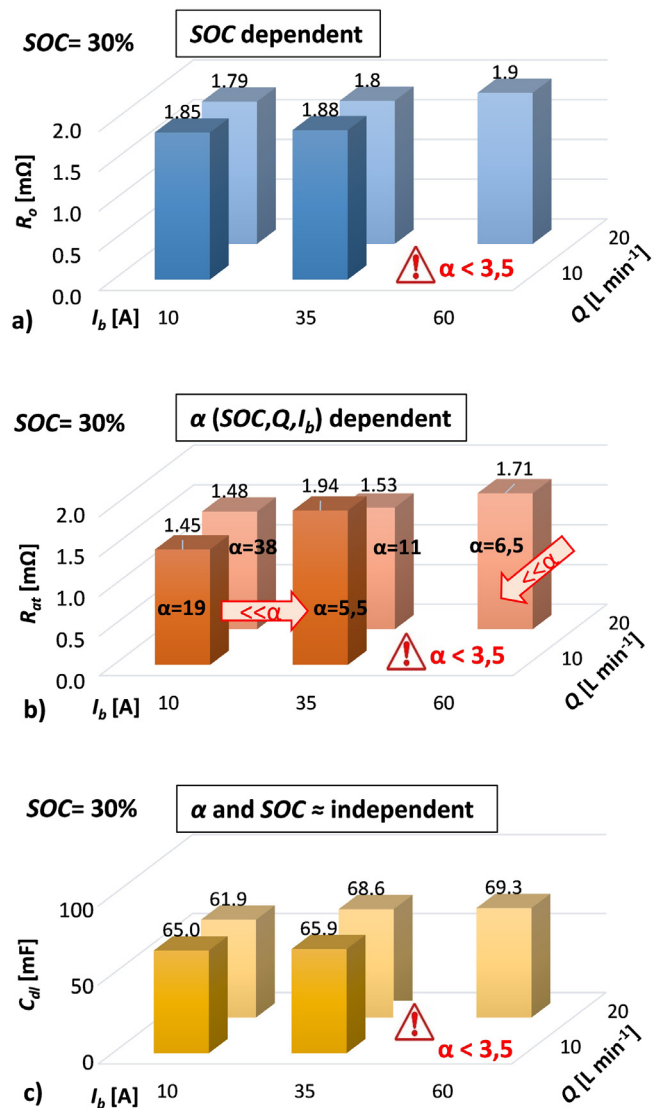
Fig. 6. Average values of the identified parameters of the IS-VRFB stack at frequency range from 0.5 Hz to 6 kHz at $SOC = 30\%$ by varying bias load current I_b and electrolyte flow rates Q, at a stimulus amplitude $I_m = 0.8$ A and constant room temperature $T = 21$ °C: (a) R_o distribution, (b) R_{at} distribution, (c) C_{dl} distribution.

cell structures (materials and assembly), proved the repeatably of the manufactured process.

Fig. 6 allows a quick gasp of I_b and Q on the identified parameters at $SOC = 30\%$. The previous considerations on R_{at} hold also at different values SOC, I_b and Q which produce values of α in a very wide range (from 5.5 to 77) inside which VRFB practical operating conditions are located. Tests at $\alpha < 3.5$ were not performed in order to avoid critical conditions related to insufficient electrolyte feeding, that may lead to improper cell reactions [55].

In all cases, numerical and experimental results were in good agreement, with a maximum error of $\pm2\%$ in the module of the impedance and $\pm25\%$ in the phase, occurring at the maximum frequency of 6 kHz, as shown in the Bode plots of Fig. 5. Such errors are sufficiently small for the aim of the analysis, considering the hurdle of the such measurements at high frequency at large VRFBs.

4.4. Steady-state dc analysis

An additional validation aimed to verify the adequacy of the equivalent circuit of Fig. 4 to describe the steady-state performance of large
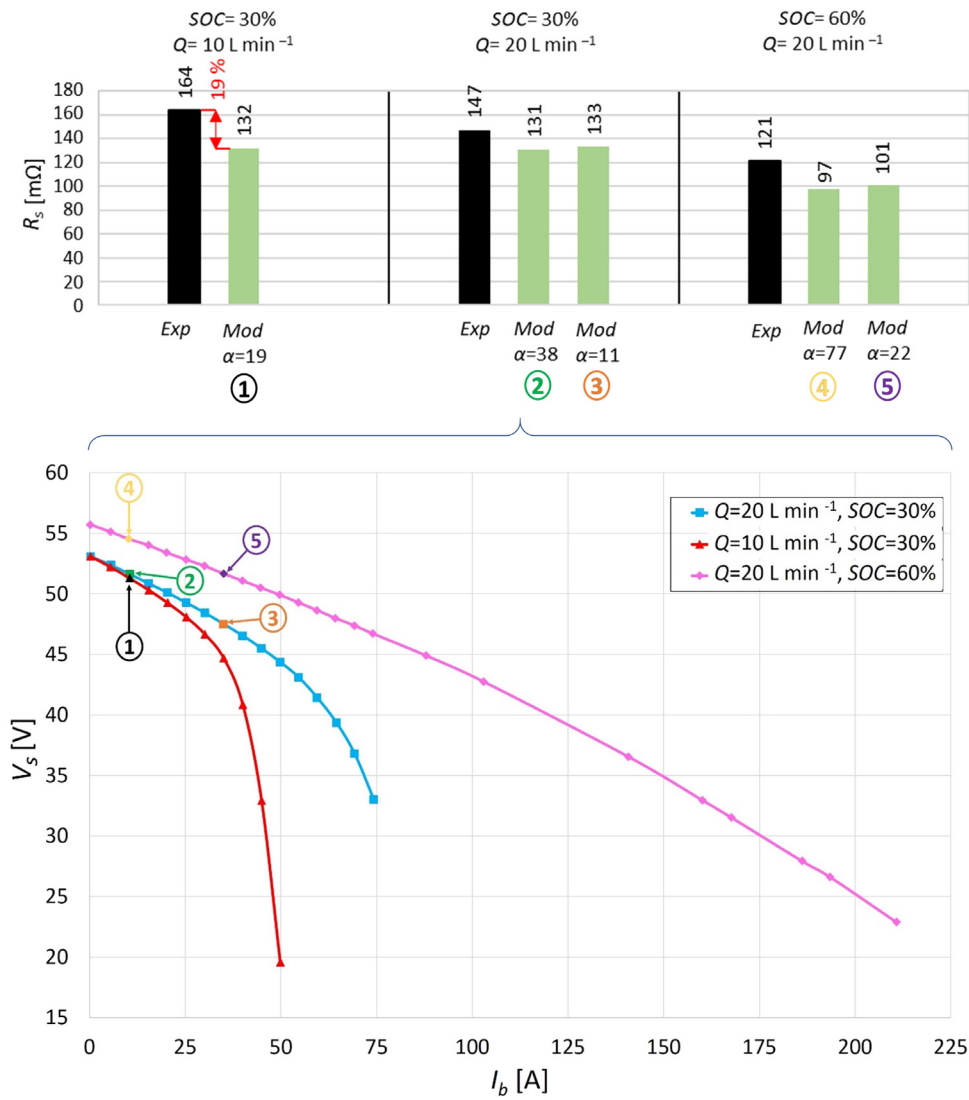
Fig. 7. Direct comparison between experimental and model ($R_o + R_{at}$) stack internal resistances in steady-state in five conditions with α between 11 and 77 (typically $\alpha \geq \alpha_k$) so that the polarization curves are dominated by ohmic losses. The temperature was kept between 20 °C and 25 °C in all tests.

VRFBs has been performed. In dc condition, the lumped circuit of Fig. 4 reduces to a dc Thévenin equivalent, whose parameters are determined as:

$$E_{0,s} = \sum_{i=1}^{N} E_{0,i} \tag{6}$$

$$R_s = \sum_{i=1}^{N} (R_{o,i} + R_{at,i}) \tag{7}$$

1   The equivalent resistance R_s obtained from the EIS measurements
2   was compared with the stack internal resistance in dc condition at the
3   same SOC and Q, which was deduced from the slope in the central
4   linear region of the polarization curves (V_s vs. I_b curve). Only the con-
5   ditions at $\alpha \geq \alpha_k$ were considered in these validations. Fig. 7 compares
6   the two internal resistances in five operating conditions at $\alpha = 11-77$,
7   whereas α_k was between 12 and 14. The maximum error between these
8   two experimental values was below 32 mΩ, with a relative error of
9   $\pm 19\%$. This results is acceptable for this kind of problems and has to be
10   attributed to the intrinsic uncertainty of the overall EIS measurement
11   chain, as argued above. In conclusion, dc measurements provided a
12   straightforward confirmation of the EIS measurements for $f \to 0$ Hz.

5. Conclusions

     The implementation of an original multichannel EIS measurement
chain at high bias currents, in a 9 kW/27 kWh VRFB, has been de-
scribed, highlighting issues and corrective actions. Stray parameters,
like wiring inductances and resistances, strongly affect the results and
made such procedure quite challenging to be implemented. On the one
hand, the battery size required longer connections which involved a
more difficult circuit optimization than similar analyses in small single
cells because they are affected by electromagnetic interferences (EMIs)
from external devices, particularly at high frequencies. On the other
hand, the stack had to be operated at high current, which generated
non-negligible conducted disturbances, which had to be properly tack-
led. A careful wiring optimization design also resorting to litz-like cable
connections and a signal configuration with a compact design partially
solved these problems. An equivalent circuit of the stack, with each
cell represented as the series of a voltage source, a linear resistor and
an RC loop, was proposed. Early results on the cell passive elements
identification by means of a numerical optimization procedure were
presented. The stack model, that is widely used in the literature in
numerical simulations evaluating the performance of large VRFB stacks,
was newer validated before. In fact, this study presents the first ex-
perimental validation on real industrial-scale VRFB stack resorting to a

multichannel EIS analyzer. With the aim of investigating how transport losses affect the circuit parameters, several tests were performed at different operating conditions in terms of battery state of charge, electrolyte flow rates and stack current, showing that only the resistance of the RC loop strongly depends on them, as widely documented in the literature in the case of single cells. The measurement methodology here presented can provide insight on arising critical conditions during battery operation and can be implemented in automatic procedures for the state of health assessment of industrial VRFB.

CRediT authorship contribution statement

Andrea Trovò: Circuit calibration, Experimental campaign and data analysis. **Walter Zamboni:** Background and literature investigation, Analysis revision. **Massimo Guarnieri:** Conceptualization, Framework definition, Experiments organization.

Declaration of competing interest

The authors declare that they have no known competing financial interests or personal relationships that could have appeared to influence the work reported in this paper.

Acknowledgment

References

[1] E. Bullich-Massagué, F.-J. Cifuentes-García, I. Glenny-Crende, M. Cheah-Mañé, M. Aragüés-Peñalba, F. Díaz-González, O. Gomis-Bellmunt, A review of energy storage technologies for large scale photovoltaic power plants, Appl. Energy 274 (2020) 115213, http://dx.doi.org/10.1016/j.apenergy.2020.115213.

[2] H. Bloomfield, D. Brayshaw, A. Troccoli, C. Goodess, M. De Felice, L. Dubus, P. Bett, Y.-M. Saint-Drenan, Quantifying the sensitivity of european power systems to energy scenarios and climate change projections, Renew. Energy 164 (2021) 1062–1075, http://dx.doi.org/10.1016/j.renene.2020.09.125.

[3] L. Das, S. Munikoti, B. Natarajan, B. Srinivasan, Measuring smart grid resilience: Methods, challenges and opportunities, Renew. Sustain. Energy Rev. 130 (2020) 109918, http://dx.doi.org/10.1016/j.rser.2020.109918.

[4] Y. Jiang, J. Fletcher, P. Burr, C. Hall, B. Zheng, D.-W. Wang, Z. Ouyang, A. Lennon, Suitability of representative electrochemical energy storage technologies for ramp-rate control of photovoltaic power, J. Power Sources 384 (2018) 396–407, http://dx.doi.org/10.1016/j.jpowsour.2018.03.013.

[5] P. Hou, P. Enevoldsen, J. Eichman, W. Hu, M.Z. Jacobson, Z. Chen, Optimizing investments in coupled offshore wind -electrolytic hydrogen storage systems in Denmark, J. Power Sources 359 (2017) 186–197, http://dx.doi.org/10.1016/j.jpowsour.2017.05.048.

[6] E. Sánchez-Díez, E. Ventosa, M. Guarnieri, A. Trovò, C. Flox, R. Marcilla, F. Soavi, P. Mazur, E. Aranzabe, R. Ferret, Redox flow batteries: Status and perspective towards sustainable stationary energy storage, J. Power Sources 481 (2021) 228804, http://dx.doi.org/10.1016/j.jpowsour.2020.228804.

[7] M. Guarnieri, P. Mattavelli, G. Petrone, G. Spagnuolo, Vanadium redox flow batteries: Potentials and challenges of an emerging storage technology, IEEE Ind. Electron. Mag. 10 (4) (2016) 20–31, http://dx.doi.org/10.1109/MIE.2016.2611760.

[8] K. Saadi, P. Nanikashvili, Z. Tatus-Portnoy, S. Hardisty, V. Shokhen, M. Zysler, D. Zitoun, Crossover-tolerant coated platinum catalysts in hydrogen/bromine redox flow battery, J. Power Sources 422 (2019) 84–91, http://dx.doi.org/10.1016/j.jpowsour.2019.03.043.

[9] M. Wu, R. Zhang, K. Liu, J. Sun, K. Chan, T. Zhao, Mesoporous carbon derived from pomelo peel as a high-performance electrode material for zinc-bromine flow batteries, J. Power Sources 442 (2019) 227255, http://dx.doi.org/10.1016/j.jpowsour.2019.227255.

[10] P. Leung, A. Shah, L. Sanz, C. Flox, J. Morante, Q. Xu, M. Mohamed, C. Ponce de León, F. Walsh, Recent developments in organic redox flow batteries: A critical review, J. Power Sources 360 (2017) 243–283, http://dx.doi.org/10.1016/j.jpowsour.2017.05.057.

[11] Vanitec transforming possibilities. Vanadium redox flow battery company, 2020, http://www.vanitec.org/vanadium-redox-flow-battery-vrfb-companies;2020a [accessed 28 October 2020].

[12] Vanitec transforming possibilities. Vanadium redox flow battery (VRFB) technology is increasingly being tested or deployed across the globe, 2020, https://willigan.digital/pr/bold-editorial/vanitec/v3/;2020b [accessed 28 October 2020].

[13] L. Arenas, C. Ponce de León, F. Walsh, Engineering aspects of the design, construction and performance of modular redox flow batteries for energy storage, J. Energy Storage 11 (2017) 119–153, http://dx.doi.org/10.1016/j.est.2017.02.007.

[14] R. Gundlapalli, S. Jayanti, Effective splitting of serpentine flow field for applications in large-scale flow batteries, J. Power Sources 487 (2021) 229409, http://dx.doi.org/10.1016/j.jpowsour.2020.229409.

[15] L.F. Arenas, C. Ponce de León, F.C. Walsh, Redox flow batteries for energy storage: their promise, achievements and challenges, Curr. Opin. Electrochem. 16 (2019) 117–126, http://dx.doi.org/10.1016/j.coelec.2019.05.007, Electrochemical Materials and Engineering - Sensors and Biosensors.

[16] Z. Xu, W. Xiao, K. Zhang, D. Zhang, H. Wei, X. Zhang, Z. Zhang, N. Pu, J. Liu, C. Yan, An advanced integrated electrode with micron- and nano-scale structures for vanadium redox flow battery, J. Power Sources 450 (2020) 227686, http://dx.doi.org/10.1016/j.jpowsour.2019.227686.

[17] M.C. Daugherty, S. Gu, D.S. Aaron, B. Chandra Mallick, Y.A. Gandomi, C.-T. Hsieh, Decorating sulfur and nitrogen co-doped graphene quantum dots on graphite felt as high-performance electrodes for vanadium redox flow batteries, J. Power Sources 477 (2020) 228709, http://dx.doi.org/10.1016/j.jpowsour.2020.228709.

[18] C. Sun, E. Negro, K. Vezzù, G. Pagot, G. Cavinato, A. Nale, Y. Herve Bang, V. Di Noto, Hybrid inorganic-organic proton-conducting membranes based on speek doped with WO3 nanoparticles for application in vanadium redox flow batteries, Electrochim. Acta 309 (2019) 311–325, http://dx.doi.org/10.1016/j.electacta.2019.03.056.

[19] J. Ye, D. Yuan, M. Ding, Y. Long, T. Long, L. Sun, C. Jia, A cost-effective nafion/lignin composite membrane with low vanadium ion permeation for high performance vanadium redox flow battery, J. Power Sources 482 (2021) 229023, http://dx.doi.org/10.1016/j.jpowsour.2020.229023.

[20] F. Jiang, W. Liao, T. Ayukawa, S.-H. Yoon, K. Nakabayashi, J. Miyawaki, Enhanced performance and durability of composite bipolar plate with surface modification of cactus-like carbon nanofibers, J. Power Sources 482 (2021) 228903, http://dx.doi.org/10.1016/j.jpowsour.2020.228903.

[21] W. Liao, F. Jiang, Y. Zhang, X. Zhou, Z. He, Highly-conductive composite bipolar plate based on ternary carbon materials and its performance in redox flow batteries, Renew. Energy 152 (2020) 1310–1316, http://dx.doi.org/10.1016/j.renene.2020.01.155.

[22] Y. Wang, Y. Zhang, L. Tang, T. Liu, J. Huang, S. Peng, X. Yang, Investigations on physicochemical properties and electrochemical performance of sulfate-chloride mixed acid electrolyte for vanadium redox flow battery, J. Power Sources 434 (2019) 226719, http://dx.doi.org/10.1016/j.jpowsour.2019.226719.

[23] N. Roznyatovskaya, J. Noack, H. Mild, M. Fühl, P. Fischer, K. Pinkwart, J. Tübke, M. Skyllas-Kazacos, Vanadium electrolyte for all-vanadium redox-flow batteries: the effect of the counter ion, Batteries 5 (1) (2019) 13.

[24] J. Huang, Y. Gao, J. Luo, S. Wang, C. Li, S. Chen, J. Zhang, Editors' Choice—Review—impedance response of porous electrodes: Theoretical framework, physical models and applications, J. Electrochem. Soc. 167 (16) (2020) 166503, http://dx.doi.org/10.1149/1945-7111/abc655.

[25] C. Gabrielli, Once upon a time there was EIS, Electrochim. Acta 331 (2020) 135324, http://dx.doi.org/10.1016/j.electacta.2019.135324.

[26] A. Lasia, Electrochemical impedance spectroscopy and its applications, Electrochemical Impedance Spectroscopy and its Applications, Springer, 2014, http://dx.doi.org/10.1007/978-1-4614-8933-7.

[27] G. Petrone, G. Spagnuolo, W. Zamboni, R. Siano, An improved mathematical method for the identification of fuel cell impedance parameters based on the interval arithmetic, Math. Comput. Simulation (2020) http://dx.doi.org/10.1016/j.matcom.2020.04.016, cited By 1.

[28] G. Petrone, W. Zamboni, G. Spagnuolo, An interval arithmetic-based method for parametric identification of a fuel cell equivalent circuit model, Appl. Energy 242 (2019) 1226–1236, http://dx.doi.org/10.1016/j.apenergy.2019.03.136.

[29] X.-Z. Yuan, C. Song, H. Wang, J. Zhang, Electrochemical impedance spectroscopy in PEM fuel cells, in: Electrochemical Impedance Spectroscopy in PEM Fuel Cells, Springer, 2010, http://dx.doi.org/10.1007/978-1-84882-846-9.

[30] U. Krewer, F. Röder, E. Harinath, R.D. Braatz, B. Bedürftig, R. Findeisen, Review—Dynamic models of Li-Ion batteries for Diagnosis and operation: A review and perspective, J. Electrochem. Soc. (2018) http://dx.doi.org/10.1149/2.1061814jes.

[31] S.M. Rezaei Niya, M. Hoorfar, Study of proton exchange membrane fuel cells using electrochemical impedance spectroscopy technique. a review, J. Power Sources 240 (2013) 281–293, http://dx.doi.org/10.1016/j.powsour.2013.04.011.

[32] M.E. Orazem, B. Tribollet, Electrochemical impedance spectroscopy, New Jersey (2008).

[33] E. Barsoukov, J.R. Macdonald (Eds.), Impedance spectroscopy: Theory, experiment, and applications - third edition, in: Impedance Spectroscopy: Theory, Experiment, and Applications - Third Edition, Wiley-Interscience, 2018, http://dx.doi.org/10.1002/0471716243.

[34] A. Fotouhi, D.J. Auger, K. Propp, S. Longo, M. Wild, A review on electric vehicle battery modelling: From Lithium-ion toward Lithium-Sulphur, in: Renewable and Sustainable Energy Reviews, 2016, http://dx.doi.org/10.1016/j.rser.2015.12.009.

[35] Q. Zheng, X. Li, Y. Cheng, G. Ning, F. Xing, H. Zhang, Development and perspective in vanadium flow battery modeling, in: Applied Energy, 2014, http://dx.doi.org/10.1016/j.apenergy.2014.06.077.

[36] S. Castano-Solis, D. Serrano-Jimenez, J. Fraile-Ardanuy, J. Sanz-Feito, Hybrid characterization procedure of li-ion battery packs for wide frequency range dynamics applications, Electr. Power Syst. Res. 166 (2019) 9–17, http://dx.doi.org/10.1016/j.epsr.2018.09.017.

[37] M. Mohamed, H. Ahmad, M.A. Seman, S. Razali, M. Najib, Electrical circuit model of a vanadium redox flow battery using extended Kalman filter, J. Power Sources 239 (2013) 284–293, http://dx.doi.org/10.1016/j.powsour.2013.03.127.

[38] Y. Zhang, J. Zhao, P. Wang, M. Skyllas-Kazacos, B. Xiong, R. Badrinarayanan, A comprehensive equivalent circuit model of all-vanadium redox flow battery for power system analysis, J. Power Sources 290 (2015) 14–24, http://dx.doi.org/10.1016/j.powsour.2015.04.169.

[39] S. Kim, E. Thomsen, G. Xia, Z. Nie, J. Bao, K. Recknagle, W. Wang, V. Viswanathan, Q. Luo, X. Wei, A. Crawford, G. Coffey, G. Maupin, V. Sprenkle, 1 kw/1 kwh advanced vanadium redox flow battery utilizing mixed acid electrolytes, J. Power Sources 237 (C) (2013) http://dx.doi.org/10.1016/j.powsour.2013.02.045.

[40] Z. Wei, K.J. Tseng, N. Wai, T.M. Lim, M. Skyllas-Kazacos, Adaptive estimation of state of charge and capacity with online identified battery model for vanadium redox flow battery, J. Power Sources 332 (2016) 389–398, http://dx.doi.org/10.1016/j.powsour.2016.09.123.

[41] Z. Wei, A. Bhattarai, C. Zou, S. Meng, T.M. Lim, M. Skyllas-Kazacos, Real-time monitoring of capacity loss for vanadium redox flow battery, J. Power Sources 390 (2018) 261–269, http://dx.doi.org/10.1016/j.powsour.2018.04.063.

[42] W. Zamboni, G. Petrone, G. Spagnuolo, D. Beretta, An evolutionary computation approach for the online/on-board identification of pem fuel cell impedance parameters with a diagnostic perspective, Energies 12 (22) (2019) 4374, http://dx.doi.org/10.3390/en12224374.

[43] C.N. Sun, F.M. Delnick, D.S. Aaron, A.B. Papandrew, M.M. Mench, T.A. Zawodzinski, Probing electrode losses in all-vanadium redox flow batteries with impedance spectroscopy, ECS Electrochem. Lett. (2013) http://dx.doi.org/10.1149/2.001305eel.

[44] C.-N. Sun, F.M. Delnick, D.S. Aaron, A.B. Papandrew, M.M. Mench, T.A. Zawodzinski, Resolving losses at the negative electrode in all-vanadium redox flow batteries using electrochemical impedance spectroscopy, J. Electrochem. Soc. (2014) http://dx.doi.org/10.1149/2.045406jes.

[45] I. Derr, M. Bruns, J. Langner, A. Fetyan, J. Melke, C. Roth, Degradation of all-vanadium redox flow batteries (VRFB) investigated by electrochemical impedance and X-ray photoelectron spectroscopy: Part 2 electrochemical degradation, J. Power Sources (2016) http://dx.doi.org/10.1016/j.powsour.2016.06.040.

[46] I. Derr, D. Przyrembel, J. Schweer, A. Fetyan, J. Langner, J. Melke, M. Weinelt, C. Roth, Electroless chemical aging of carbon felt electrodes for the all-vanadium redox flow battery (VRFB) investigated by electrochemical impedance and X-ray photoelectron spectroscopy, Electrochim. Acta 246 (2017) 783–793, http://dx.doi.org/10.1016/j.electacta.2017.06.050.

[47] A.M. Pezeshki, R.L. Sacci, F.M. Delnick, D.S. Aaron, M.M. Mench, Elucidating effects of cell architecture, electrode material, and solution composition on overpotentials in redox flow batteries, Electrochim. Acta 229 (2017) 261–270, http://dx.doi.org/10.1016/j.electacta.2017.01.056.

[48] M. Becker, T. Turek, Combination of impedance spectroscopy and potential probe sensing to characterize vanadium redox-flow batteries, J. Power Sources 446 (2020) 227349, http://dx.doi.org/10.1016/j.powsour.2019.227349.

[49] M. Messaggi, C. Rabissi, C. Gambaro, L. Meda, A. Casalegno, M. Zago, Investigation of vanadium redox flow batteries performance through locally-resolved polarisation curves and impedance spectroscopy: Insight into the effects of electrolyte, flow field geometry and electrode thickness, J. Power Sources 449 (2020) 227588, http://dx.doi.org/10.1016/j.powsour.2019.227588.

[50] Y. Li, J. Bao, M. Skyllas-Kazacos, M.P. Akter, X. Zhang, J. Fletcher, Studies on dynamic responses and impedance of the vanadium redox flow battery, Appl. Energy (2019) http://dx.doi.org/10.1016/j.apenergy.2019.01.015.

[51] D. Manschke, T. Seipp, S. Berthold, K.A. Friedrich, Verification of redox flow batteries' functionality by electrochemical impedance spectroscopy tests, Batteries (2018) http://dx.doi.org/10.3390/batteries4040058.

[52] M. Guarnieri, A. Trovò, A. D'Anzi, P. Alotto, Developing vanadium redox flow technology on a 9-kw 26-kwh industrial scale test facility: Design review and early experiments, Appl. Energy 230 (2018) 1425–1434, http://dx.doi.org/10.1016/j.apenergy.2018.09.021.

[53] A. Trovò, M. Guarnieri, Standby thermal management system for a kw-class vanadium redox flow battery, Energy Convers. Manage. 226 (2020) 113510, http://dx.doi.org/10.1016/j.enconman.2020.113510.

[54] A. Trovò, M. Guarnieri, Battery management system with testing protocols for kw-class vanadium redox flow batteries, in: 2020 2nd IEEE International Conference on Industrial Electronics for Sustainable Energy Systems (IESES), Vol. 1, 2020, pp. 33–38, http://dx.doi.org/10.1109/IESES45645.2020.9210697.

[55] A. Trovò, Battery management system for industrial-scale vanadium redox flow batteries: Features and operation, J. Power Sources 465 (2020) 228229, http://dx.doi.org/10.1016/j.powsour.2020.228229.

[56] M. Guarnieri, A. Trovò, G. Marini, A. Sutto, P. Alotto, High current polarization tests on a 9 kw vanadium redox flow battery, J. Power Sources 431 (2019) 239–249, http://dx.doi.org/10.1016/j.powsour.2019.05.035.

[57] C.R. Sullivan, Optimal choice for number of strands in a litz-wire transformer winding, IEEE Trans. Power Electron. 14 (2) (1999) 283–291, http://dx.doi.org/10.1109/63.750181.

[58] M. Pavelka, F. Wandschneider, P. Mazur, Thermodynamic derivation of open circuit voltage in vanadium redox flow batteries, J. Power Sources 293 (2015) 400–408, http://dx.doi.org/10.1016/j.powsour.2015.05.049.

[59] M. Guarnieri, A. Trovò, F. Picano, Enhancing the efficiency of kw-class vanadium redox flow batteries by flow factor modulation: An experimental method, Appl. Energy 262 (2020) 114532, http://dx.doi.org/10.1016/j.apenergy.2020.114532.

[60] F. Béguin, E. Raymundo-Piñero, E. Frackowiak, Electrical Double-Layer Capacitors and Pseudocapacitors, CRC Press, Boca Raton, FL, 2010.

[61] A. Trovò, F. Picano, M. Guarnieri, Comparison of energy losses in a 9 kw vanadium redox flow battery, J. Power Sources 440 (2019) 227144, http://dx.doi.org/10.1016/j.powsour.2019.227144.

[62] N. Meddings, M. Heinrich, F. Overney, J.-S. Lee, V. Ruiz, E. Napolitano, S. Seitz, G. Hinds, R. Raccichini, M. Gaberšček, J. Park, Application of electrochemical impedance spectroscopy to commercial li-ion cells: A review, J. Power Sources 480 (2020) 228742, http://dx.doi.org/10.1016/j.powsour.2020.228742.

[63] M. Guarnieri, E. Negro, V.D. Noto, P. Alotto, A selective hybrid stochastic strategy for fuel-cell multi-parameter identification, J. Power Sources 332 (2016) 249–264, http://dx.doi.org/10.1016/j.powsour.2016.09.131.

[64] N. Poli, M. Schäffer, A. Trovò, J. Noack, M. Guarnieri, P. Fischer, Novel electrolyte rebalancing method for vanadium redox flow batteries, Chem. Eng. J. 405 (2021) 126583, http://dx.doi.org/10.1016/j.cej.2020.126583.

[65] D. Maggiolo, F. Zanini, F. Picano, A. Trovò, S. Carmignato, M. Guarnieri, Particle based method and X-ray computed tomography for pore-scale flow characterization in vrfb electrodes, Energy Storage Mater. 16 (2019) 91–96, http://dx.doi.org/10.1016/j.ensm.2018.04.021.

[66] X. Li, J. Xiong, A. Tang, Y. Qin, J. Liu, C. Yan, Investigation of the use of electrolyte viscosity for online state-of-charge monitoring design in vanadium redox flow battery, Appl. Energy 211 (2018) 1050–1059, http://dx.doi.org/10.1016/j.apenergy.2017.12.009.